

Bridging the Gap Between Concrete Microstructures and Tunnel Linings

E. Binder, H. Wang, T. Schlappal, J.L. Zhang, Y. Yuan,
B. Pichler and H.A. Mang

Abstract The title of this work represents a figurative counterpart of bridging the topographical gap between Hongkong and Macao. Presently under construction, the bridge that connects these two cities at opposite sides of the mouth of the Pearl River is interrupted by a submersed tunnel, which is the actual research object of this paper. By means of four different topics in the framework of the general subject of this contribution, reflected by its title, the scientific progress resulting from multiscale structural analyses of tunnel linings is documented. The four topics are: (a) microstructural analysis of impact and blast loading in tunnel linings, (b) multiscale analysis of thermal stresses in concrete linings due to sudden temperature changes, (c) experiments and finite element modeling of concrete hinges in Mechanized Tunneling, and (d) multiscale structural analysis of a segmented tunnel ring.

1 Introduction

The title of this work follows the one of a research project, sponsored by the Austrian Science Fund. It reads as “Bridging the gap by means of multiscale structural analysis” [1]. The ambitious goal of this project, in which the authors of this contribution are involved, is quantification of the added value of multiscale analyses, notwithstanding the explicit acknowledgment of scientific progress that manifests itself in such analyses. The overriding research object is the 35.6 km long Hongkong-Zhuhai-Macao Bridge, presently under construction. For shipping, the bridge is interrupted by a 5.7 km long tunnel below the bottom of the sea, representing the actual research object. Figure 1 shows the course of the bridge. Figure 2 refers to the tunnel, which is located between the West Artificial Island and the East Artificial Island (see Fig. 1). A figurative counterpart of bridging the topographical gap between Hongkong and

E. Binder · H. Wang · T. Schlappal · J.L. Zhang · Y. Yuan ·
B. Pichler · H.A. Mang (✉)
TU Wien – Vienna University of Technology, Karlsplatz 13/202,
1040 Vienna, Austria
e-mail: herbert.mang@tuwien.ac.at

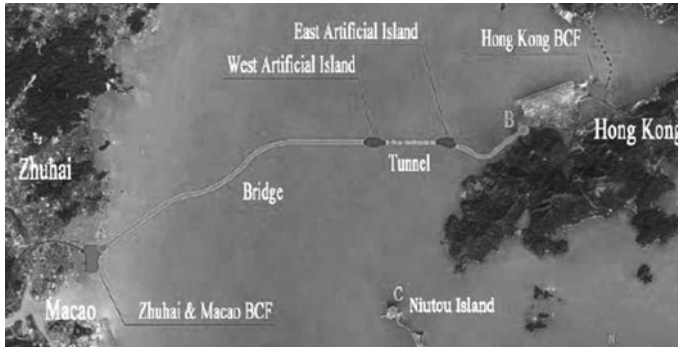


Fig. 1 Course of the Hongkong-Zhuhai-Macao-Bridge [1]

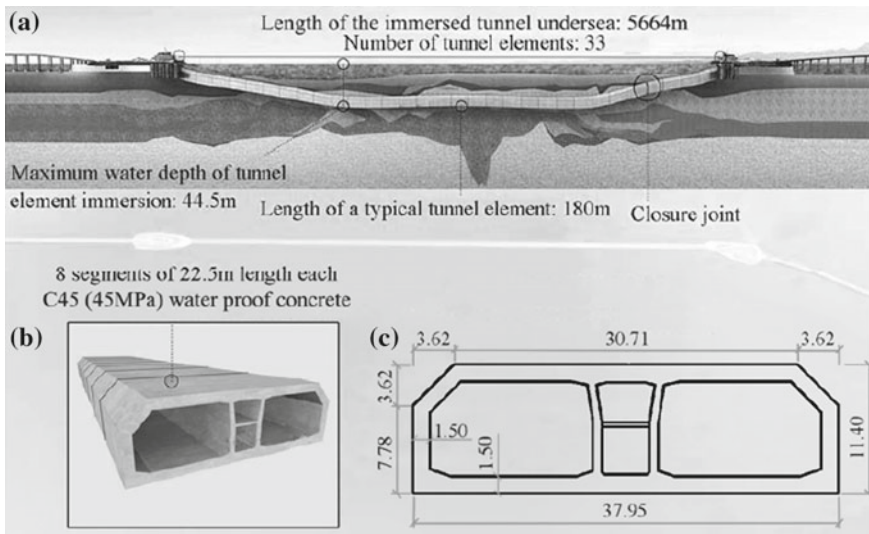
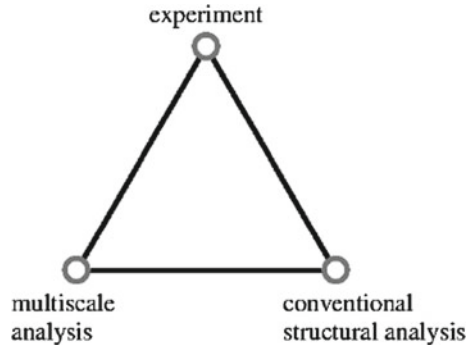


Fig. 2 Tunnel between the West Artificial Island and the East Artificial Island (see Fig. 1). Tunnel: **a** longitudinal section, **b** typical tunnel element, **c** cross-section of a tunnel element [1]

Macao is the bridging of several orders of magnitude in multiscale structural analyses. The intended assessment of the added value of such analyses requires a triad of related results (see Fig. 3). The focus of the scientific work in the first half of the aforementioned research project, which was started in Fall of 2015, has been on multiscale analyses of tunnel linings. Selected results of this research work are presented in this contribution.

Fig. 3 Triad of results, required for assessing the added value of multiscale analyses of tunnel linings [1]



2 Organization of the Paper

In the framework of the general subject of this paper the following four topics are treated: (a) Microstructural analysis of impact and blast loading in tunneling (Sect. 3), (b) Multiscale analysis of thermal stresses in concrete linings due to sudden temperature changes (Sect. 4), (c) Experiments and FE modeling of concrete hinges in Mechanized Tunneling (Sect. 5), (d) Multiscale structural analysis of a segmented tunneling ring (Sect. 6). Section 7 contains a summary of this work, conclusions drawn from the underlying research.

3 Microstructural Analysis of Impact and Blast Loading in Tunneling

Current safety standards require that tunnels withstand exceptional loading events such as e.g. impact and blast loads. Such events may result from traffic accidents, e.g. from cars crashing into a tunnel lining, or from the detonation of Improvised Explosive Devices. This has been the motivation to investigate concrete subjected to high-dynamic loading rates. It is well known from the large database of available test results that the strength of cementitious materials increases with increasing loading rate. This strengthening is significant in the high dynamic testing regime, where strain rates are typically larger than 1 s^{-1} . The available experimental database has resulted in several modeling attempts. The CEB-recommendation [2], the model of Tedesco and Ross [3], and the model of Grote et al. [4] provide empirical formulae for the high-dynamic compressive strength of cementitious materials. Mihashi and Wittmann [5] as well as Bažant et al. [6] have developed models, based on the assumption that micro-cracking depends on the strain rate. Cotsovos and Pavlovic [7], Li and Meng [8], and Gary and Bailly [9] have attributed the strength increase with increasing strain rate to inertial confinement, which is a structural effect.

Table 1 Experimental data from high-dynamic strength tests by Kühn et al. [11]

Specimen properties: $f_{sta} = 25.1 \text{ MPa}$ $E = 32 \text{ GPa}$ $\nu = 0.2$					
$h = 80 \text{ mm}$ $\varnothing = 50 \text{ mm}$ $a_{max} = 8 \text{ mm}$ $\rho = 2400 \text{ kg/m}^3$					
$\dot{\varepsilon} \text{ [s}^{-1}\text{]}$	136.6	150.1	185.5	190.0	202.7
$f_{dyn} \text{ [MPa]}$	95.1	104.2	119.2	125.7	142.5

Fischer et al. [10] have explained dynamic strengthening based on the quasi-static strength and the duration of the failure process, lasting from the start of crack propagation to the disintegration of the tested specimen. Herein, the latter model is extended towards consideration of uncertainty regarding the quasi-static strength. It is used to re-analyze a recent high-dynamic test series on concrete, see Table 1 and [11].

3.1 Prediction of High-Dynamic Strength, Based on Quasi-Static Strength Data

3.1.1 Statistical Scatter of Quasi-Static Strength Values

While test repetitions are desirable in experimental mechanics in order to quantify the dispersion of the investigated material properties, many researchers carry out just one test, or they communicate only the mean value of results from several tests. In both cases an estimation of statistical quantiles is impossible. As a remedy, it is proposed herein to follow the Eurocode and to consider compressive strength values of concrete to scatter according to a Gaussian distribution. In addition, the Eurocode defines the characteristic strength for ultimate limit state design as the 5%-quantile of the strength distribution. Concerning the compressive strength of concrete, the 5%-quantile is introduced as by 8 MPa smaller than the mean strength determined in laboratory testing. This approach is related to a standard deviation of the uniaxial compressive strength amounting to $\hat{s} = 4.865 \text{ MPa}$.

Considering the compressive strength as a positive quantity, a lognormal distribution is more appropriate to describe statistical properties. In order to convert the standard deviation of the Eurocode to the one of the envisioned lognormal distribution, it is proposed to set the 5%-quantile of the Gaussian distribution equal to the 5%-quantile of the lognormal distribution. Denoting the mean strength value from the experiments as \hat{f} and the standard deviation of the Eurocode as \hat{s} , the proposed approach yields the sought standard deviation of the lognormal distribution as

$$\bar{s}(\hat{s}, \hat{f}) = u(5\%) + \sqrt{u(5\%)^2 - 2 \cdot \ln \left(1 + \frac{u(5\%) \cdot \hat{s}}{\hat{f}} \right)} \quad , \quad (1)$$

where $u(5\%) = -1.645$ is the value that cuts an area of 5% of the standardized normal distribution, exhibiting a vanishing mean value. Based on the standard deviation of the lognormal distribution according to Eq.(1), any p -quantile of the lognormal distribution can be quantified according to the following standard relation:

$$f(p) = \exp \left(\ln(\hat{f}) + u(p) \cdot \bar{s} \right). \quad (2)$$

3.1.2 High-Dynamic Strength Modeling, Considering Uncertainty of the Failure Mode

The present contribution follows Fischer et al. who developed a model for the dynamic increase factor (DIF) of the compressive strength of cementitious materials, see [10]. Herein, the model is extended towards consideration of the experimental dispersion of the quasi-static strength. Furthermore, it is shown that re-analysis of high-dynamic strength tests requires careful consideration of the failure mechanism. Along this line of research, it is assumed that macroscopic cracking starts—also under high-dynamic compressive loading—once the stress level has reached the quasi-static strength, and that the ultimate load of the specimen is reached, once the first crack has propagated through the entire specimen such that it disintegrates into pieces. In this context, it is noteworthy that the speed of cracks, propagating along nanoscopic material interfaces, is equal to the Rayleigh wave speed [12], which is only a little smaller than the shear wave velocity v_s . With the static strength f_{sta} , Young's modulus E , and the strain rate $\dot{\epsilon}$, the DIF (dynamic strength increase factor) is obtained as

$$DIF = \frac{f_{dyn}}{f_{sta}} = 1 + \frac{\dot{\epsilon} \cdot E}{f_{sta}} \cdot \frac{l_c}{v_s}. \quad (3)$$

In Eq. (3), l_c stands for the relevant crack propagation length. It is equal to the length along which the relevant crack must propagate in order to split the sample. Therefore, l_c depends on the geometrical properties of the tested specimen. Considering that axial splitting is the typical failure mode under uniaxial compression, the ultimate load sustained by the specimen is reached, once the crack size is equal to the height h of the specimen. Realistic scenarios are bounded by the following two cases: (a) if the relevant crack starts right at the interface between the specimen and the load plate, the crack will grow along the total height h of the specimen, and (b) if cracking starts at the center of the specimen, two crack edges will propagate simultaneously, and each of them will cover a length equal to $h/2$.

According to the previous explanation, the dispersion of the high-dynamic strength values results from two sources: (a) the uncertainty regarding the quasi-static strength, see f_{sta} in Eq. (3) as well as Sect. 3.1.1, and (b) the uncertainty regarding the position from which the relevant crack starts to propagate, see l_c in Eq. (3). These uncertainties result in intervals of possible strength values, which are

quite wide in the quasi-static regime, but form a rather narrow band in the high-dynamic regime. When comparing Eq. (3) with experimental data, the only free parameter is the relevant crack propagation length l_c . It can be optimized such that model-predicted DIF values, DIF_{pred} , agree in the best-possible fashion with their experimental counterparts, DIF_{exp} , according to

$$E_{tot} = \left| \frac{1}{n} \sum_{i=1}^n \frac{DIF_{pred,i} - DIF_{exp,i}}{DIF_{exp}^{mean}} \right| \rightarrow \min. \quad (4)$$

In Eq. (4), n denotes the number of experimentally determined DIF values, and E_{tot} stands for the total prediction error.

3.2 Model Application to High-Dynamic Strength Data

In this contribution the model validation is extended to high-dynamic strength tests performed by Kühn et al. [11] on concrete specimens. In the following, Eq. (3) is used to analyze the experimental data, listed in Table 1. Kühn et al. specify the specimen properties, listed in Table 1, and provided images showing the remaining fragments of specimens after testing, see Fig. 4. Presumably, the remaining cone-shaped fragments, with a height about one half of the specimen height, are caused by a confinement, resulting from friction in the contact area between the specimen and the pressure bar.

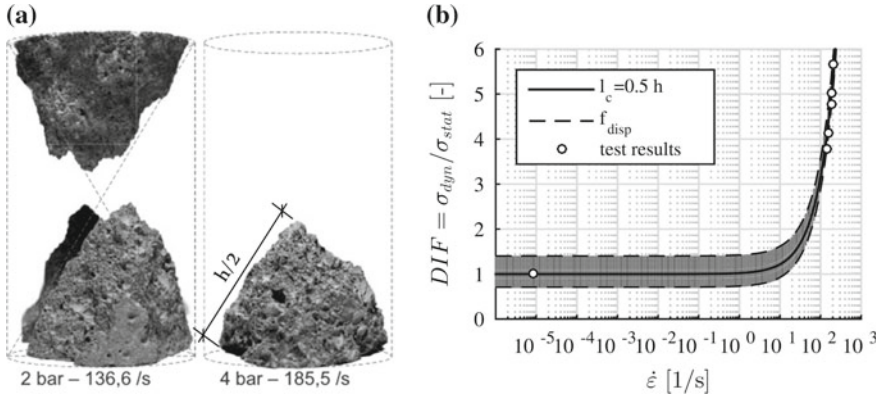


Fig. 4 **a** Illustration of the specimen fragments from [11], **b** validation of the model for high-dynamic strength increase according to Eq. (3): comparison of measured dynamic strength-increase factors from Kühn et al. [11] with corresponding model predictions obtained for the specimen properties listed in Table 1, and for $h = 80$ mm

The remaining fragments of the specimen show that cracks had to propagate along a length $l_c \approx h/2$ in order to split the specimen, see Fig. 4a. Using this length together with properties of the tested specimen (Table 1) as input for Eq. (3) yields model predictions that agree very well with the experimental data, see the solid line in Fig. 4b. The uncertainty regarding the quasi-static strength manifests itself in Fig. 4b in the form of the dashed boundary lines.

3.3 Conclusions

The present study suggests that the propagation length, required for the first crack to split a specimen under high-dynamic compression, has a great influence on the ultimate load of the tested specimen. As for modeling, it was assumed that also for high-dynamic loading, crack propagation starts at the quasi-static strength and that the ultimate load sustained by the tested specimen increases with increasing propagation length, required for the first crack to split the specimen. It is concluded that, no matter how short a stress pulse exceeding the quasi-static strength may be, tunnel linings will be damaged. Therefore, they need to be inspected carefully even after non-catastrophic high-dynamic loading events. Furthermore, the model allows to estimate the depth of the damage zone, provided the duration of the stress pulse is known. It is equal to the period of time, during which the stress is larger than the quasi-static strength, multiplied by the crack propagation speed, i.e. by the shear wave velocity.

4 Multiscale Analysis of Thermal Stresses in Concrete Linings Due to Sudden Temperature Changes

A change of the temperature of a concrete structure induces thermal eigenstrains. In general, they result in thermal stresses which may lead to cracking of the material. Instationary heat conduction, i.e. transient heat conduction, inevitably activates *macroscopic* thermal stresses. Kinematic constraints, preventing temperature-induced deformations, also result in thermal stresses. Furthermore, the mismatch of the thermal expansion coefficients of the concrete constituents (cement paste matrix and aggregate inclusions) [13] gives rise to *microscopic* self-equilibrated stresses, even if the concrete volume is free of macroscopic kinematic constraints.

A model for multiscale thermo-mechanical analysis is presented. Bottom-up homogenization of the concrete allows for upscaling of elastic stiffnesses and of thermal expansion coefficients of the concrete constituents. The resulting homogenized properties of concrete serve as input for macroscopic thermal stress analysis. Top-down stress concentration in turn provides access to microscopic thermal stresses in the cement paste and the aggregates, as functions of both the macroscopic stresses and a mismatch of microscopic thermal expansion coefficients. The proposed model

is applied to stress analysis of a 3-D simply-supported concrete beam, subjected to 1-D heat conduction.

4.1 Multiscale Thermo-Mechanical Model of Concrete

Concrete is a matrix-inclusion composite, consisting of a cement paste matrix and aggregate inclusions. Homogenized material properties of concrete, such as the stiffness and the thermal expansion coefficient, are related to the corresponding properties of the constituents.

As the temperature increases (or decreases), the cement paste and the aggregates expand (or contract) in accordance to their coefficients of thermal expansion, inducing eigenstrains $\boldsymbol{\epsilon}_{cp}^e$ and $\boldsymbol{\epsilon}_{agg}^e$, reading as

$$\boldsymbol{\epsilon}_{cp}^e = \alpha_{cp} \Delta T \mathbf{1}, \quad \boldsymbol{\epsilon}_{agg}^e = \alpha_{agg} \Delta T \mathbf{1}, \quad (5)$$

where α_{cp} and α_{agg} are the thermal expansion coefficients of the cement paste and the aggregates, respectively. Corresponding eigenstresses of the cement paste and the aggregates can be computed as

$$\boldsymbol{\sigma}_{cp}^e = -\mathbb{C}_{cp} : \boldsymbol{\epsilon}_{cp}^e, \quad \boldsymbol{\sigma}_{agg}^e = -\mathbb{C}_{agg} : \boldsymbol{\epsilon}_{agg}^e, \quad (6)$$

where \mathbb{C}_{cp} and \mathbb{C}_{agg} are the elastic stiffness tensors of the cement paste and the aggregates, respectively. The transition to the macroscopic scale of concrete is provided by Levin's theorem [14], containing the macroscopic stress tensor $\boldsymbol{\Sigma}_{con}$, the macroscopic strain tensor \boldsymbol{E}_{con} , and the macroscopic eigenstrain and eigenstress tensors \boldsymbol{E}_{con}^e and $\boldsymbol{\Sigma}_{con}^e$ as

$$\boldsymbol{\Sigma}_{con} = \mathbb{C}_{con} : (\boldsymbol{E}_{con} - \boldsymbol{E}_{con}^e) = \mathbb{C}_{con} : \boldsymbol{E}_{con} + \boldsymbol{\Sigma}_{con}^e, \quad (7)$$

with the homogenized stiffness tensor reading as

$$\mathbb{C}_{con} = f_{cp} \mathbb{C}_{cp} : \mathbb{A}_{cp} + f_{agg} \mathbb{C}_{agg} : \mathbb{A}_{agg}, \quad (8)$$

and with the homogenized eigenstress tensor reading as

$$\boldsymbol{\Sigma}_{con}^e = f_{cp} \boldsymbol{\sigma}_{cp}^e : \mathbb{A}_{cp} + f_{agg} \boldsymbol{\sigma}_{agg}^e : \mathbb{A}_{agg}, \quad (9)$$

where f_{cp} and f_{agg} are the volume fractions of the cement paste and the aggregates in the concrete, and \mathbb{A}_{cp} and \mathbb{A}_{agg} are the strain concentration tensors of the cement paste and the aggregates, which are estimated by means of the Mori-Tanaka method [15].

As for relating the thermal expansion coefficient of concrete, α_{con} , to the thermal expansion coefficients of the constituents, i.e. to α_{cp} and α_{agg} , it is assumed that

concrete can deform freely, such that the macroscopic stress tensor vanishes. For this scenario, Eq. (7) yields

$$\boldsymbol{\Sigma}_{con} = 0 \Rightarrow \mathbf{E}_{con} = \mathbf{E}_{con}^e = -\mathbb{C}_{con}^{-1} : \boldsymbol{\Sigma}_{con}^e. \quad (10)$$

The sought expression for α_{con} is obtained by setting \mathbf{E}_{con} in Eq. (10) equal to $\alpha_{con} \Delta T \mathbf{1}$ and inserting (5) into (6), followed by substituting the resulting expression into (9), and, finally, by substituting the outcome together with (8) into (10). This delivers, after division by ΔT ,

$$\begin{aligned} \alpha_{con} \mathbf{1} &= [f_{cp} \mathbb{C}_{cp} : \mathbb{A}_{cp} + f_{agg} \mathbb{C}_{agg} : \mathbb{A}_{agg}]^{-1} \\ &: [\alpha_{cp} f_{cp} (\mathbb{C}_{cp} : \mathbf{1}) : \mathbb{A}_{cp} + \alpha_{agg} f_{agg} (\mathbb{C}_{agg} : \mathbf{1}) : \mathbb{A}_{agg}]. \end{aligned} \quad (11)$$

The thermal expansion coefficient α_{con} from Eq. (11) intervenes in macroscopic thermal analysis of concrete structures.

After thermal analysis of a concrete structure, the macrostress $\boldsymbol{\Sigma}_{con}$ and the temperature change ΔT are known at every point of the structure. The scale transition to the cement paste and the aggregates at all structural points is carried out as follows: starting from the temperature change ΔT and combining Eqs. (5), (6), and (9), delivers the homogenized eigenstress tensor $\boldsymbol{\Sigma}_{con}^e$. Inserting the latter together with Eq. (8) into Eq. (7) allows for quantifying the macroscopic strains \mathbf{E}_{con} . The auxiliary strain \mathbf{E}_{∞} , representing the remote loading of the Eshelby problems, is given in [15]. Then, the strains $\boldsymbol{\varepsilon}_{cp}$ and $\boldsymbol{\varepsilon}_{agg}$ are quantified as

$$\boldsymbol{\varepsilon}_{cp} = \mathbf{E}_{\infty}, \quad \boldsymbol{\varepsilon}_{agg} = [\mathbb{I} + \mathbb{P} : (\mathbb{C}_{agg} - \mathbb{C}_{cp})] : [\mathbf{E}_{\infty} - \mathbb{P} : (\boldsymbol{\sigma}_{agg}^e - \boldsymbol{\sigma}_{cp}^e)]. \quad (12)$$

The stresses $\boldsymbol{\sigma}_{cp}$ and $\boldsymbol{\sigma}_{agg}$ finally follow from the elasticity laws as

$$\boldsymbol{\sigma}_{cp} = \mathbb{C}_{cp} : (\boldsymbol{\varepsilon}_{cp} - \boldsymbol{\varepsilon}_{cp}^e), \quad \boldsymbol{\sigma}_{agg} = \mathbb{C}_{agg} : (\boldsymbol{\varepsilon}_{agg} - \boldsymbol{\varepsilon}_{agg}^e). \quad (13)$$

4.2 Multiscale Thermo-Mechanical Analysis of a Simply-Supported Concrete Beam Subjected to Sudden Cooling

4.2.1 Analytical Solution of Heat Conduction Problem

Multiscale thermo-mechanical analysis is carried out for a simply-supported concrete beam with a rectangular cross-section. Initially, the beam exhibits a uniform temperature field, denoted as the reference temperature T_{ref} , i.e.

$$T(z, t = 0) = T_{ref}. \quad (14)$$

The structure is loaded by sudden cooling of the top surface, $z = h$, to zero-degree centigrade, while the temperature at the bottom surface, $z = 0$, the beam remains at T_{ref} , i.e.

$$T(z = h, t) = 0^\circ\text{C}, \quad T(z = 0, t) = T_{ref}. \quad (15)$$

Consideration of thermal insulation of the lateral surfaces results in 1-D heat conduction along the height of the beam, i.e. along the z -direction. Therefore, the heat equation reads as

$$\frac{\partial T}{\partial t} - a \frac{\partial^2 T}{\partial z^2} = 0, \quad (16)$$

where a represents the thermal diffusivity of concrete.

The analytical solution of the heat conduction problem, defined in Eqs. (14)–(16), is obtained as follows [16]:

$$T(z, t) = T_{ref} \left[\left(1 - \frac{z}{h}\right) + \sum_{n=1}^{\infty} \frac{2(-1)^{n-1}}{n\pi} \sin\left(\frac{n\pi z}{h}\right) \exp\left(-\frac{n^2\pi^2 a t}{h^2}\right) \right]. \quad (17)$$

4.2.2 Macroscopic and Microscopic Thermal Stress Analysis

A 3-D FE model of a simply-supported beam with the dimensions $l \times b \times h = 2 \text{ m} \times 0.4 \text{ m} \times 0.3 \text{ m}$ is chosen for thermo-mechanical analysis. The stiffness tensor and the thermal expansion coefficient of concrete are predicted by means of the established multiscale model of concrete, see Eqs. (8) and (11).

The beam is loaded by temperature distributions according to Eq. (17), referring to the dimensionless time instants $at/h^2 \in [1, 10^{-1}, 10^{-2}]$, with $a = 4.73 \times 10^{-7} \text{ m}^2/\text{s}$. The distribution of the normal stresses along the height of the cross-section in the middle of the beam, $\Sigma_{xx}(z)$, is shown in Fig. 5a. Large thermal stresses are obtained right after sudden cooling. They gradually decrease and finally vanish, as the temperature profile along the height of the beam approaches the linear distribution. Tensile stresses appear close to the top and bottom surfaces of the beam, while compressive stresses prevail in its middle part. Notably, because of overall equilibrium of the structure, stress resultants in the form of a normal force and a bending moment vanish at all instants of time.

Microscopic stresses in the cement paste and the aggregates are quantified by the established multiscale model, with the macroscopic stress tensor and the temperature distribution along the height of the beam as input. The average stresses in the cement paste matrix and in the aggregate inclusions at the dimensionless time instant $at/h^2 = 10^{-1}$ are shown in Fig. 5b. Compared to the aggregates, the tensile stresses in the cement paste are larger, which increases the risk of microcracking of the cement paste.

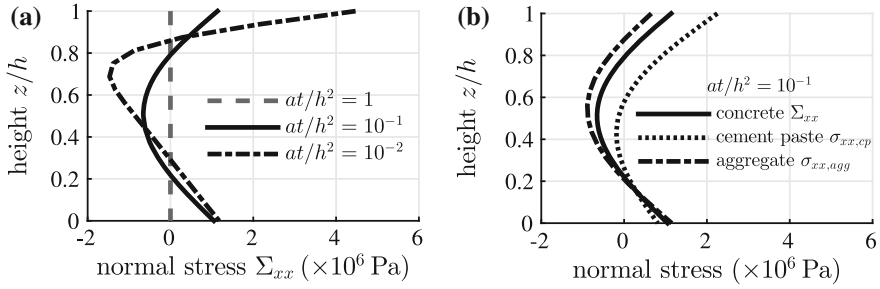


Fig. 5 Evaluation of **a** the macroscopic normal stresses Σ_{xx} for dimensionless time instants $at/h^2 \in [1, 10^{-1}, 10^{-2}]$ and **b** the normal stresses of the homogenized concrete, the cement paste and the aggregates at $at/h^2 = 10^{-1}$, along the height of the cross-section in the middle of the beam

4.3 Conclusions

A model for multiscale thermo-mechanical analysis of concrete structures was proposed and applied to a simply-supported concrete beam, subjected to 1-D heat conduction. Considerable temperature-induced tensile stresses develop right after the time instant of sudden cooling. Thereafter, they gradually decrease and finally vanish, as the heat conduction approaches the steady-state regime. Since the thermal expansion coefficient of the cement paste is typically much larger than the one of the aggregates, the cement paste matrix exhibits tensile stresses which are (a) larger than the ones of the aggregates and (b) larger than the overall macroscopic stresses of concrete. Therefore, the presented mode of multiscale modeling is highly recommended for analysis focusing on the possibility of cracking of concrete tunnel linings under thermal loading.

5 Experiments and FE Modeling of Concrete Linings in Mechanized Tunneling

Primary linings in Mechanized Tunneling are made of precast reinforced concrete segments. Such linings contain both longitudinal and circumferential segment-to-segment interfaces which are referred to as concrete hinges. The linings are subjected to external loads, resulting from the ground pressure and from the tunnel boring machine. The overall safety of segmented linings is strongly related to the integrity of segment-to-segment interfaces, which have to transmit both normal forces and bending moments. The resulting relative rotation angles are of prime interest for designers who typically rely on formulae by Gladwell [17] or Janßen [18]. Notably, Janßen's formulae were derived from older ones by Leonhardt and Reimann [19], who developed design guidelines for concrete hinges used in integral bridge construction. However, these guidelines refer to serviceability conditions, i.e. they do not provide information on the bearing capacity of concrete hinges. This is the motivation for the present contribution.

5.1 Experimental Data from Testing of Concrete Hinges

The structural behavior of concrete hinges under eccentric compression was recently studied by Schlappal et al. [20]. In the following, information is provided on the materials and on the chosen geometric dimensions of the concrete hinges, furthermore, on the test setup and on test results from eccentric compression up to the bearing capacity. Notably, throughout this work compression is considered by a positive sign.

5.1.1 Materials and Test Specimens

The three tested concrete hinges were made of steel-reinforced concrete. Concrete C 35/45 was produced with a commercial cement, Viennese tap water, and with calcite aggregates with a maximum size of 16 mm. The cube compressive strength, $f_{c,cube} = 56.25$ MPa, and Young's modulus, $E = 34.75$ GPa, were determined 28 days after production, following the Austrian standards for testing of concrete. The steel quality of the rebars was chosen as B550 A.

The geometric shape of the tested concrete hinges complied with the design guidelines of Leonhardt and Reimann [19]. The overall width amounted to 25 cm, the height to 35 cm, and the depth to 40 cm, see Fig. 6a. The depth of the lateral and the front-side notches amounted to 8.75 cm and 5 cm, respectively. Therefore, the cross-section of the neck was equal to 7.5×30 cm², see Fig. 6a. At the top and the bottom of the concrete hinges, steel plates of two centimeter thickness were provided. They ensured an effective distribution of the concentrated external line loads. Each steel plate was welded to the neighboring reinforcement cage. The top and bottom reinforcement cages were in turn connected by three pairs of crossed steel rebars with cross-over points right at the center of the neck, see Fig. 6a.

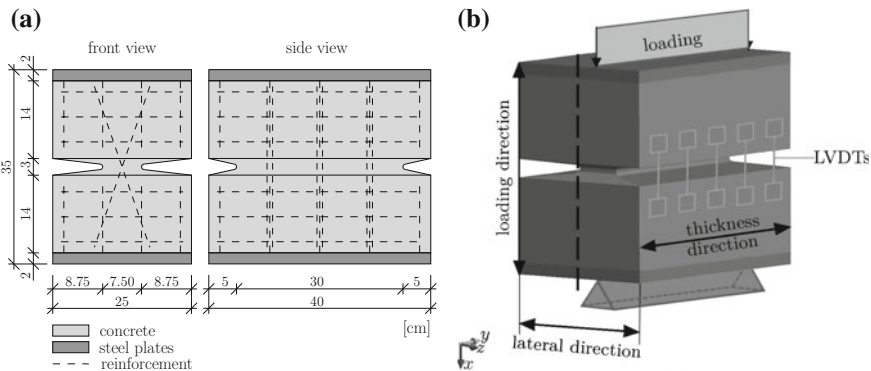


Fig. 6 **a** Geometric dimensions [20] and **b** boundary conditions [21] of the tested reinforced concrete hinges

5.1.2 Test Setup

The tests consisted of three nominally identical concrete hinges that were subjected, one after another, to eccentric line loads, see Fig. 6b. This resulted in combined compression and bending, whereby the bending moment M was equal to the applied normal force N , times the eccentricity e :

$$M = N e. \quad (18)$$

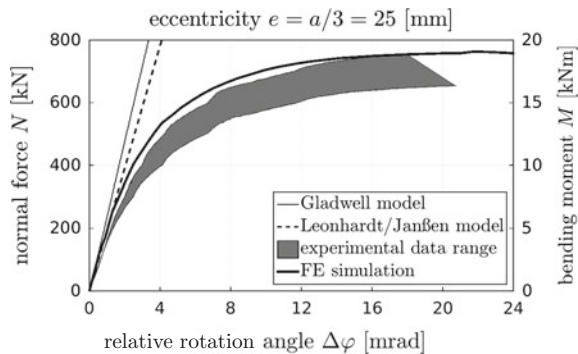
As for quantification of the displacements, inductive displacement sensors (LVDTs) were mounted at the lateral surfaces of the concrete hinges. They permitted measuring changes of the notch mouth opening displacements of the lateral notches.

As for studying the development of tensile cracking as a function of e and N , a reasonable value of e had to be defined. In this context, the design guidelines of Leonhardt and Reimann [19] were followed. They are applicable to eccentricities up to as $a/3 = 25$ mm, where a denotes the width of the neck. The guidelines take into account that for $\max e = a/3$ tensile cracking will extend across half of the neck width, i.e. right to the center of the concrete hinge.

5.1.3 Eccentric Compression up to the Bearing Capacity

The measured relation between the increasing eccentric normal force and the corresponding relative rotation angle of the concrete hinges is shown in Fig. 7. Once the normal force exceeded 200 kN, the relative rotation angle increased superlinearly with increasing loading. When it exceeded 15 mrad, the loading could no longer be increased significantly. The bearing capacity of each one of the three tested concrete hinges was equal to approximately 700 kN. This refers to a bending moment, equal to approximately 17.5 kNm, see Eq. (18), considering $e = 25$ mm.

Fig. 7 Comparison of measurements from eccentric compression tests [20] with numerical results from three-dimensional FE simulations [21] and with relationships by Gladwell [17], Leonhardt and Reimann [19], and Janßen [18]



5.2 FE Simulations of the Tested Concrete Hinges

The experimental observations, described in Sect. 5.1, were analyzed by means of the FEM by Kalliauer et al. [21]. Geometrically linear FE simulations were performed in order to gain insight into the structural behavior of concrete hinges, based on quantification of stress states *inside* their volume, which is typically inaccessible in experimental testing.

5.2.1 2-D FE Simulations for Quantification of the Stress Triaxiality in the Neck Region

In order to gain insight into the triaxiality of the compressive stresses in the neck region, 2-D FE simulations were carried out, considering a plane strain state in the x-z plane containing the center of the concrete hinge (Fig. 6b). The characteristic ratio of the principal stresses in the neck region was 1.00 : 0.45 : 0.30. The characteristic triaxial compressive stress state σ can be formulated as

$$\sigma = \sigma_\ell \cdot \left[1.00 \mathbf{e}_x \otimes \mathbf{e}_x + 0.45 \mathbf{e}_y \otimes \mathbf{e}_y + 0.30 \mathbf{e}_z \otimes \mathbf{e}_z \right], \quad (19)$$

where σ_ℓ denotes the principal compressive normal stress in the loading direction. This confinement results in a significant strengthening of concrete relative to its uniaxial compressive strength.

5.2.2 Micromechanics-Assisted Updating of Input Parameters for 3-D FE Simulations

3-D FE simulations based on default input values do not deliver quantitatively reliable results. In particular, the initial structural stiffness and the bearing capacity are overestimated. This indicates pre-existing damage of the concrete hinges. Model updating consists of identifying suitable values of Young's modulus, the uniaxial tensile strength, the fracture energy, and the triaxial compressive strength. In order to reduce the number of free parameters from four to two, a multiscale model for tensile softening of concrete was used [22]. It establishes quantitative links between the increasing crack density, on the one hand, and the corresponding reductions of the elastic stiffness, the tensile strength, and the fracture energy of concrete, on the other hand. This results in micromechanics-assisted FE simulations of concrete hinges. In addition, pre-existing damage indicates the necessity to reduce the *triaxial* compressive strength of concrete. This can be achieved by increasing the input parameter λ_t , which quantifies the ratio between the *auxiliary* uniaxial tensile strength f'_t of the Men  trety-Willam failure surface and the *actual* uniaxial tensile strength f_t of the Rankine failure surface. Based on the default input parameter $\lambda_t = 2$, the Men  trety-Willam failure surface suggests that the triaxial compressive strength $\sigma_{\ell u}$ is equal

to 5.65 times the uniaxial compressive strength. Increasing the value of the input parameter λ_t in the framework of sensitivity analysis, delivers Men  trety-Willam failure surfaces with decreasing slopes in the $\xi - \rho$ diagrams, where by ξ and ρ are proportional to the first invariant of the stress tensor and to the square-root of the second invariant of the stress deviator, respectively. It is found that $\lambda_t = 8.5$ allows for reproducing the experimentally obtained bearing capacity of the tested concrete hinges in a qualitatively and quantitatively satisfactory fashion, see Fig. 7.

5.3 Conclusions

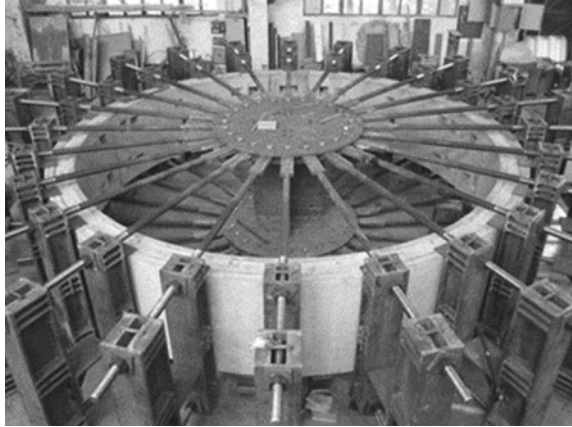
Researchers working in Mechanized Tunneling are interested in relative rotation angles, developing across concrete necks, subjected to compression and bending. Models with predictive capacity are needed in order to develop powerful simulation tools for segmented tunnel linings. To support such a development, a combined experimental-computational study on concrete hinges subjected to eccentric compression was performed. FE simulations allowed for quantifying the *triaxial* compressive stress state prevailing in the neck region and for reproducing the nonlinear structural behavior right up to the bearing capacity. Existing guidelines do not consider the nonlinear behavior of concrete hinges under eccentric compression, see the linear functions in Fig. 7. The presented research results are expected to support the future development of a structural simulation tool for segmented tunnel linings.

6 Multiscale Structural Analysis of a Segmented Tunnel Ring

A real-scale test of a segmented tunnel ring, see Fig. 8, which was carried out at Tongji University [23], is re-analyzed. The tested ring consisted of 6 reinforced concrete segments. The diameter of the ring amounted to 6.2 m. The ring was subjected to anisotropic loading, imposed by 24 hydraulic jacks up to the Ultimate Limit State (ULS). The convergences in both the vertical and the horizontal direction as well as the displacement/rotation discontinuities at the interfaces of the segments were measured. Cracking of concrete was observed during the test.

The test provided valuable insight into the progressive failure and the bearing capacity of segmented tunnel linings. However, real-scale tests on segmented tunnel rings are expensive and time-consuming. This was the motivation for the development of a structural analysis model, reproducing real-scale tests. To this end, a multiscale model for concrete [22] and transfer relations for structural analysis of segmented tunnel rings [24] are combined, resulting in multiscale structural analysis of such rings.

Fig. 8 Setup of a real-scale test of a segmented tunnel ring at Tongji University [23]



6.1 Multiscale Model of Concrete

The microstructure of the concrete is considered to be hierarchically organized in six length scales, i.e. the solid calcium-silicate-hydrates (C-S-H), the hydrate gel, the hydrate foam, the cement paste, the mortar, and the concrete. The elastic stiffness and the fracture energy of the C-S-H, known from molecular dynamics simulations documented in the literature, are upscaled via the hierarchically-organized scales to the material scale of concrete [22]. In this way, Young's modulus, Poisson's ratio, and the tensile strength of the homogenized concrete are obtained as [25]

$$E_c^{hom} = 43.57 \text{ GPa} , \quad (20)$$

$$\nu_c^{hom} = 0.2424 , \quad (21)$$

$$f_t = 3.17 \text{ MPa} . \quad (22)$$

6.2 Hybrid Analysis of the Segmented Tunnel Ring, Based on Transfer Relations

The transfer relations express the vector of the state variables at an arbitrary cross-section with the angular coordinate φ as the product of a transfer matrix and the vector of the state variables at the initial cross-section (index "i") $\varphi_i = 0$. They read as [24]

$$\begin{bmatrix} u(\varphi) \\ v(\varphi) \\ \theta(\varphi) \\ M(\varphi) \\ N(\varphi) \\ V(\varphi) \\ 1 \end{bmatrix} = \begin{bmatrix} \cos \varphi & \sin \varphi & T_{13}(\varphi) & T_{14}(\varphi) & T_{15}(\varphi) & T_{16}(\varphi) & \sum u^L(\varphi) \\ -\sin \varphi & \cos \varphi & T_{23}(\varphi) & T_{24}(\varphi) & T_{25}(\varphi) & T_{26}(\varphi) & \sum v^L(\varphi) \\ 0 & 0 & 1 & T_{34}(\varphi) & T_{35}(\varphi) & T_{36}(\varphi) & \sum \theta^L(\varphi) \\ 0 & 0 & 0 & 1 & T_{45}(\varphi) & T_{46}(\varphi) & \sum M^L(\varphi) \\ 0 & 0 & 0 & 0 & \cos \varphi & -\sin \varphi & \sum N^L(\varphi) \\ 0 & 0 & 0 & 0 & \sin \varphi & \cos \varphi & \sum V^L(\varphi) \\ 0 & 0 & 0 & 0 & 0 & 0 & 1 \end{bmatrix} \begin{bmatrix} u_i \\ v_i \\ \theta_i \\ M_i \\ N_i \\ V_i \\ 1 \end{bmatrix}, \quad (23)$$

where u , v , and θ stand for the radial displacement, the tangential displacement, and the cross-sectional rotation, respectively; M , N , and V are the bending moment, the axial force, and the shear force, respectively; EI , EA , and R denote the bending stiffness, the extensional stiffness, and the radius of the neutral axis of the arch, respectively. Notably, the complete list of the nonzero elements of the transfer matrix T_{ij} is available in [24]. The top six elements of the last column of the transfer matrix in Eq. (23) contain so-called load integrals, representing the solutions for the radial point loads and for the interfacial dislocations. As an example, the load integral of the radial displacement for a radial point load P reads as [24]:

$$u^L(\varphi) = \frac{1}{2} \left(\frac{PR}{EA} + \frac{PR^3}{EI} \right) \left[(\varphi - \varphi_p) \cos(\varphi - \varphi_p) - \sin(\varphi - \varphi_p) \right] H(\varphi - \varphi_p), \quad (24)$$

where P and φ_p denote the jack force and its circumferential position, respectively, and $H(\varphi - \varphi_p)$ stands for the Heaviside function. The load integral of the radial displacement for interfacial discontinuities happening at circumferential position ϕ_j reads as [24]:

$$u^L(\varphi) = \left[\Delta u_j \cos(\varphi - \varphi_j) + \Delta v_j \sin(\varphi - \varphi_j) + R \Delta \theta_j \sin(\varphi - \varphi_j) \right] H(\varphi - \varphi_j), \quad (25)$$

where Δu_j , Δv_j and $\Delta \theta_j$, are the interfacial discontinuities of the radial displacement, the circumferential displacement, and the cross-sectional rotation, respectively. The expressions for the remaining five load integrals are also available in [24]. The prescribed point loads, P , the measured interfacial displacement/rotation discontinuities, Δu_j , Δv_j , $\Delta \theta_j$, and φ_j , appearing in the load integrals, e.g. Eqs. (24) and (25), serve as input for the “hybrid analysis”.

The state variables at the initial cross-section are determined as follows: Measuring φ from the middle cross-section of the crown segment and specifying the transfer relations (23) for $\varphi = 2\pi$ provides a relation between the vectors of the state variables at the initial and the final (index “f”) cross-section. The compatibility of the deformations of the *closed* ring requires $u_f = u_i$, $v_f = v_i$, $\theta_f = \theta_i$. These three conditions permit determination of the static variables at the initial cross-section, i.e. of M_i , N_i , and V_i . The kinematic state variables at the initial cross-section, u_i , v_i , and θ_i , refer to rigid body motions. Therefore, they may be set equal to zero or to arbitrary non-zero values.

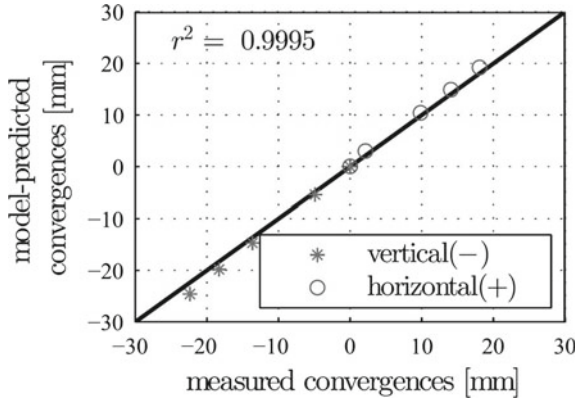


Fig. 9 Comparison of the convergences obtained from the simulation and the measurements [24]

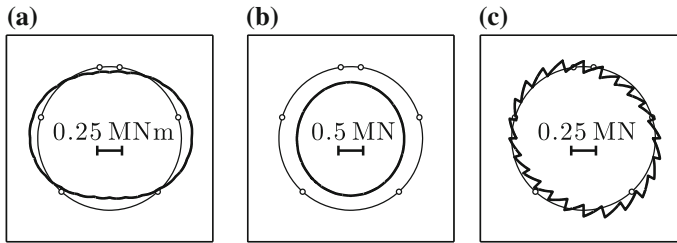


Fig. 10 Analysis results referring to the 4th load step at which cracking of concrete started: **a** bending moment distribution; **b** axial force distribution; **c** shear force distribution [24]

In order to validate the simulation approach, the normal stresses of the concrete and the two orthogonal convergences are computed and compared to the experimental results. The computed stresses exceed the tensile strength of concrete (see Eq. (22)) at the 4th load step, which agrees perfectly well with the corresponding experimental observation that cracking was first observed at this load step [23]. This proves the usefulness of the model. In addition, the model-predicted convergences agree very well with measurements, as follows from the quadratic correlation coefficient, amounting to $r^2 = 0.9995$, see Fig. 9. Notably, this comparison is a non-trivial assessment of the predictive capabilities of the model, (a) since the experimentally measured convergences are independent of the input of the model, and (b) since the model does not involve any fitted parameters.

Figure 10 shows the distributions of the bending moments, the axial forces, and the shear forces along the axis of the ring. Figure 11 illustrates the deformed configuration of the segmented tunnel and the stress-to-strength ratio of concrete [24].

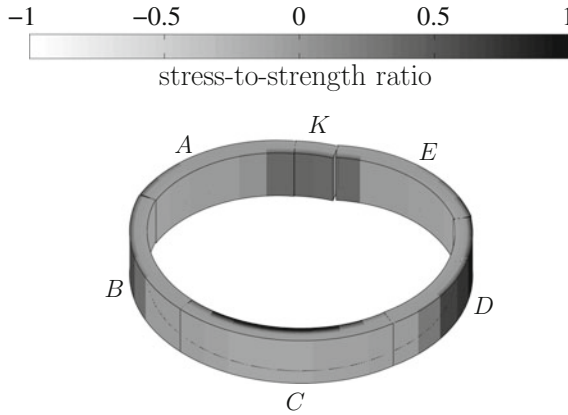


Fig. 11 Deformed configuration and stress-to-strength ratio of concrete at the 4th load step; the magnification factors of the cross-sectional dimensions and the displacements are 1 and 100, respectively [24]

6.3 Conclusions

A multiscale micro-fracture-mechanics model permits upscaling of the elastic stiffness and the tensile strength from the molecular to the material scale. “Hybrid analysis” provides a shortcut to avoid the challenge of conventional structural analysis, involving identification of the constitutive relations of the interfaces between the segments. Up to the stage of concrete cracking, the proposed analysis approach reproduced the experimental observations. It increases the insight into the structural behavior of the tested tunnel ring.

The present work is viewed as the first step towards a multiscale-hybrid method for the design of segmented tunnel linings. In order to consider cracking in a straightforward manner, a softening law of concrete on the basis of micro-fracture-mechanics is desirable. As for design-oriented calculations, the interfacial dislocations are unknown. The development of a reliable model of the interfacial behavior is a topic of ongoing research, see also Sect. 5.

7 Summary and Conclusions

The structural behavior of tunnel linings is strongly influenced by the material behavior of concrete. The latter results etiologically from thermo-hygro-chemo-mechanical processes, occurring at the microstructure of the hierarchically organized material. This is the motivation for multiscale structural analysis, which aims at relating the *causes* at microstructural material scales to the *effects* at macrostructural scales of tunnel linings. It consists of three steps: (a) Identification of the microstructural

processes, influencing the structural behavior. (b) Upscaling of the microstructural processes to the material scale of concrete. (c) Performing structural simulations, based on multiscale models of concrete. The four topics addressed in the present contribution are related to different stages of multiscale structural analysis.

Concrete failure under impact loading refers to crack propagation along nanoscopic material interfaces [10, 26]. Cracking starts, once the static strength is reached. The speed of the crack propagation is equal to the Rayleigh wave speed [12]. During cracking, i.e. during the evolution of concrete failure, the impact load can be further increased, thus resulting in high-dynamic strengthening. In the present contribution, the probabilistic version of the described multiscale model was successfully applied to re-analysis of a series of high-dynamic tests regarding the uniaxial compressive strength of concrete [11].

When concrete is subjected to temperature changes, homogenization techniques for eigenstrains are used for scale transitions [15]. Mismatching thermal expansion coefficients of the cement paste and the aggregates, respectively, are upscaled to the effective thermal expansion coefficient of the concrete. Stresses imposed on the concrete are downscaled to average stresses of the cement paste and the aggregates, respectively. Applying this model in the context of multiscale structural analysis, it was shown that sudden cooling of a concrete structure is particularly harmful, because tensile stresses are concentrated in the cement paste, thus increasing the risk of cracking of concrete.

Multiscale structural analysis may be carried out with standard FE software and the phenomenological material models implemented therein. This became possible by involving a multiscale model for tensile failure of concrete, which uses a crack density parameter as the damage variable. The model establishes relations between the Young's modulus, the tensile strength, and the fracture energy of concrete. This enables a significant reduction of fitting parameters in the typical case that default FE input values do not allow for reproducing the measured structural behavior reliably, thus raising the need for model updating techniques.

Multiscale structural analysis was also applied to a real-scale test on a segmented tunnel ring. Stiffness and strength of the concrete were quantified by means of the aforementioned multiscale material model. As for the structural analysis, the prescribed external loading *and* the measured discontinuities of displacements/rotations at the segment-to-segment interfaces served as input for analytically derived transfer relations for circular segmented tunnel linings. This allowed for a hybrid analysis of the experiment without the need to describe the nontrivial behavior of the segment-to-segment interfaces.

Acknowledgements Financial support by the Austrian Science Fund (FWF), provided within project P 281 31-N32 Bridging the Gap by Means of Multiscale Structural Analyses, is gratefully acknowledged. Interesting discussions with J. Kalliauer and M. Ausweger and support by them are also gratefully acknowledged.

References

1. H.A. Mang, Bridging the gap by means of multiscale structural analyses. Research project supported by the Austrian Science Fund (FWF) P281, 31–N32 (2015)
2. Comité Euro-International du Béton, CEB-FIP Model Code (1993)
3. J.W. Tedesco, C.A. Ross, Strain-rate-dependent constitutive equations for concrete. *J. Press. Vessel Technol.* **120**, 398–405 (1998)
4. D.L. Grote, S.W. Park, M. Zhou, Dynamic behavior of concrete at high strain rates and pressure: I. Experimental characterization. *Int. J. Impact Eng.* **25**(9), 869–886 (2001)
5. H. Mihashi, F.H. Wittmann, Stochastic approach to study the influence of rate of loading on strength of concrete. *Heron* **25** (1980)
6. Z.P. Bazant, F.C. Caner, M.D. Adley, S.A. Akers, Fracturing rate effect and creep in microplane model for dynamics. *J. Eng. Mech.* **126**, 962–970 (2000)
7. D.M. Cotsovos, M.N. Pavlovic, Numerical investigation of concrete subjected to compressive impact loading. Part 1: a fundamental explanation for the apparent strength gain at high loading rates. *Comput. Struct.* **86**, 145–163 (2008)
8. Q.M. Li, H. Meng, About the dynamic strength enhancement of concrete-like materials in a split Hopkinson pressure bar test. *Int. J. Solid Struct.* **40**, 343–360 (2003)
9. G. Gary, P. Bailly, Behaviour of quasi-brittle material at high strain rate. experiment and modelling. *Eur. J. Mech. A/Solid* **17**(3), 403–420 (1998)
10. I. Fischer, B. Pichler, E. Lach, C. Turner, E. Barraud, F. Britz, Compressive strength of cement paste as a function of loading rate: experiments and engineering mechanics analysis. *Cem. Concr. Res.* **58**, 186–200 (2014)
11. T. Kühn, C. Steinke, Z. Sile, I. Zreid, M. Kaliske, M. Curbach, Dynamische Eigenschaften von Beton im Experiment und in der Simulation (Dynamic properties of concrete in experiments and simulations). *Beton-und Stahlbeton* **111** (2016)
12. F.F. Abraham, H. Gao, How fast can cracks propagate? *Phys. Rev. Lett.* **84**(14), 3113–3116 (2000)
13. J.K. Emanuel, J.L. Hulse, Prediction of the thermal coefficient of expansion of concrete. *ACI J.* **74**, 149–155 (1977)
14. V.M. Levin, Coefficients of temperature expansion of heterogeneous materials. *Mekha. Tverd. Tela* **2**, 83–94 (1967)
15. B. Pichler, C. Hellmich, Estimation of influence tensors for eigenstressed multiphase elastic media with nonaligned inclusion phases of arbitrary ellipsoidal shape. *J. Eng. Mech.* **136**, 1043–1053 (2010)
16. M. Ausweger, Spannungen und Verformungen gerader Einzelstäbe zufolge Temperaturbeanspruchung (Stresses and deformation of straight beams resulting from temperature changes). Bachelor thesis, Vienna University of Technology, Austria (2016)
17. G.M. Gladwell, *Contact Problems in the Classical Theory of Elasticity* (Springer Science & Business Media, 1980)
18. P. Janßen, Tragverhalten von Tunnelausbauten mit Gelenktübbings (Structural behavior of segmented tunnel linings) Ph.D. thesis, Technical University of Braunschweig, Germany, 1986
19. F. Leonhardt, H. Reimann, Betongelenke (Concrete hinges). *Dtsch. Ausschuss für Stahlb.* **175**, 1–33 (1965). German
20. T. Schlappal, M. Schweigler, S. Gmainer, M. Peyerl, B. Pichler, Creep and cracking of concrete hinges—Insight from centric and eccentric experiments. *Mat. Struct. Under Review* (2017)
21. J. Kalliauer, T. Schlappal, M. Vill, H.A. Mang, B. Pichler, Bearing capacity of concrete hinges subjected to eccentric compression—Multiscale structural analysis of experiments. *Acta Mech.* Accepted for Publication (2017)
22. M. Hlobil, M. Göstl, J. Burrus, C. Hellmich, B. Pichler, Molecular-to-macro upscaling of concrete fracture: theory and experiments. *J. Mech. Phys. Sol.* Under Revision
23. X. Liu, Y. Bai, Y. Yuan, H.A. Mang, Experimental investigation of the ultimate bearing capacity of continuously-jointed segmental tunnel linings. *Struct. Infrastruct. E* **12**, 1–16 (2016)

24. J.L. Zhang, C. Vida, Y. Yuan, C. Hellmich, H.A. Mang, B. Pichler, A hybrid analysis method for displacement-monitored segmented circular tunnel rings. Eng. Struct. Accepted for Publication (2017)
25. J.L. Zhang, H.A. Mang, X. Liu, Y. Yuan, B. Pichler, Hybrid multiscale analysis of the bearing capacity of a segmented tunnel ring
26. B. Pichler, I. Fischer, E. Lach, C. Turner, E. Barraud, F. Britz, The influence of loading rate on the compressive strength of cementitious materials: experiments and separation of time scales-based analysis, in *Computational Modeling of Concrete Structures, Proceedings of Euro-C*, vol 2 (2014), pp. 731–739

<http://www.springer.com/978-3-319-60884-6>

Advances in Computational Plasticity

A Book in Honour of D. Roger J. Owen

Oñate, E.; Peric, D.; de Souza Neto, E.; Chiumenti, M.

(Eds.)

2018, XVII, 434 p. 241 illus., 170 illus. in color.,

Hardcover

ISBN: 978-3-319-60884-6